References

AMOROS, J. L. & AMOROS, M. (1968). *Molecular Crystals: Their Transforms and Diffuse Scattering*. New York: Wiley.

KITAIGORODSKY, A. I. (1973). *Molecular Crystals and Molecules*. New York, London: Academic Press.

MATSUSHIMA, N. & HIKICHI, K. (1978). *Polym. J.* **10**, 437–441.

TSVANKIN, D. YA., LEVIN, V. JU., PAPKOV, V. S., ZHUKOV, V. P., ZHDANOV, A. A. & ANDRIANOV, K. A. (1979). *Vysokomol. Soedin. Ser. A*, **21**, 2126–2135.

WILLIS, B. T. M. & PRYOR, A. W. (1975). *Thermal Vibrations in Crystallography*. Cambridge Univ. Press.

Acta Cryst. (1982). A**38**, 310–317

High-Resolution Images of Ordered Alloys by High-Voltage Electron Microscopy

BY D. SHINDO

The Research Institute for Iron, Steel and Other Metals, Tohoku University, Sendai, Japan

(*Received* 10 *September* 1981; *accepted* 17 *November* 1981)

Abstract

The image formation of high-voltage, high-resolution electron microscopy of ordered alloys has been studied on the basis of many-beam dynamical diffraction theory. It is revealed that superstructure images are observable for a rather thick crystal when nearly kinematical relationships hold among certain beams of the superlattice reflections; these beams are almost in phase and have amplitudes proportional to their structure factors. Thickness dependences of the phase differences and the scattering amplitudes are calculated for the superstructure of $D0_{23}$ type of the gold-based alloys Au_3X (X = Mg, Zn and Cd). The results are discussed in connection with the difference in atomic scattering factors of the constituents X. The contrast of the superstructure image is discussed in terms of the amplitude–phase diagram of the superlattice reflections.

I. Introduction

The many-beam imaging technique has been developed for high-resolution electron microscopy to investigate structures of crystalline and amorphous materials (Iijima, 1971). Amelinckx and his colleagues have made extensive high-resolution studies on ordered alloys using 100 kV electron microscopes [Amelinckx, 1978–79; Van Tendeloo, 1980]. The many-beam imaging technique with the use of a 1 MV electron microscope has been applied to the study of superstructures of gold-based alloys with Cd, Mn and Mg (Hiraga, Hirabayashi & Shindo, 1977; Hiraga, Shindo, Hirabayashi, Terasaki & Watanabe, 1980; Terasaki, Watanabe, Hiraga, Shindo & Hirabayashi, 1980). In these observations, the solute atom positions projected along the incident beam appear as either bright or dark dots, and can be identified at the atomic level from comparison with the calculations based on dynamical diffraction theory. In this respect, high-voltage, high-resolution electron microscopy [HVHREM] is a powerful means for the investigation of ordered structures (Hirabayashi, 1980; Hirabayashi, Hiraga & Shindo, 1981).

High-resolution images which are interpretable in terms of ordered atomic arrangements are called superstructure images (Hiraga, Shindo & Hirabayashi, 1981). These images do not reflect a projection of crystal potential itself, which may be interpreted in the weak-phase-object approximation, but exhibit the atom columns of constituent B in A_3B alloys projected down along the incident beam. The superstructure images are contributed dominantly by superlattice reflections rather than fundamental reflections.

We have observed previously the superstructure images of Au–Cd alloys of several hundred ångströms thickness. In the successive experiments on such alloys as Au–Mg, Au–Mn and Au–Zn, however, we noticed that the superstructure images were not always observable for foils as thick as in the case of the Au–Cd alloy. It is worthwhile, therefore, to clarify the theoretical background for the formation of superstructure images of ordered alloys. In this paper, we first deal with the dynamical electron scattering from ordered alloys using the multislice formulation (Cowley & Moodie, 1957; Cowley, 1975). Then we examine the amplitude of superlattice reflections as a function of crystal thickness for the superstructure of $D0_{23}$ or Al_3Zr type (space group $I4/mmm$) of Au_3X alloys (X = Mg, Zn and Cd). Finally we discuss the contrast of superstructure images in terms of the amplitude–phase diagram of superlattice reflections.

0567-7394/82/030310-08$01.00

II. Dynamical electron scattering from ordered alloys

We consider an ordered alloy with orthogonal axes. A hypothetical electron diffraction pattern of the alloy is illustrated in Fig. 1. Dynamical scattering effects on a superlattice reflection may be described taking into account three assemblies of scattering vectors $\{U_1\}$, $\{U_2\}$ and $\{U_3\}$: $\{U_1\}$ correspond to the scattering from fundamental reflections, $\{U_2\}$ the scattering from superlattice reflections with the reciprocal-lattice vectors for fundamental reflections, and $\{U_3\}$ the scattering from superlattice reflections with the reciprocal-lattice vectors for superlattice reflections. The vectors $\mathbf{u}_2^s$, $\mathbf{u}^f$ and $\mathbf{u}_3^s$ in Fig. 1 are components of $\{U_1\}$, $\{U_2\}$ and $\{U_3\}$, respectively, for the superlattice reflection S_2. The superscripts s and f refer to superlattice and fundamental reflections, respectively. There is a relationship between the superlattice reflections S_1 and S_2,

$$\mathbf{u}_2^s = \mathbf{u}^f + \mathbf{u}_1^s. \tag{1}$$

According to the multislice formulation for dynamical electron diffraction theory, the wave function of a diffracted beam at the nth crystal slice is written as

$$\Psi_n(\mathbf{u}) = \{\Psi_{n-1}(\mathbf{u})\, P(\mathbf{u})\} * Q(\mathbf{u}), \tag{2}$$

where $P(\mathbf{u})$ is the propagation function and $Q(\mathbf{u})$ is the transmission function (Cowley, 1975). $P(\mathbf{u})$ is given as

$$P(\mathbf{u}) = \exp(\pi i \Delta z |\mathbf{u}|^2), \tag{3}$$

where λ is the wavelength of the incident electron and Δz is the thickness of one crystal slice. In the weak-phase-object approximation, the transmission function is given as

$$\begin{aligned} Q(\mathbf{u}) &= \mathscr{F}[\exp(i\sigma\varphi(\mathbf{r})\,\Delta z)] \\ &\simeq \mathscr{F}[1 + i\sigma\varphi(\mathbf{r})\,\Delta z], \end{aligned} \tag{4}$$

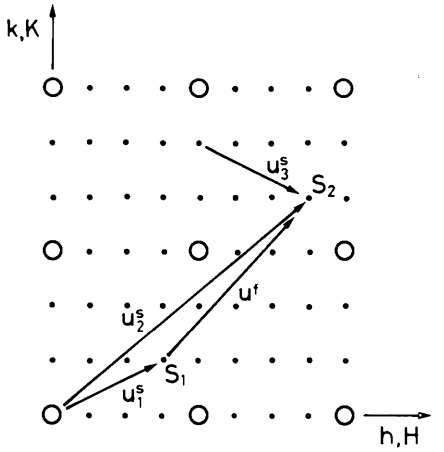

Fig. 1. Schematic representation of a section of reciprocal lattice for an ordered alloy. Open circles and small dots indicate fundamental and superlattice reflections, respectively.

where σ is the interaction constant and $\varphi(\mathbf{r})\,\Delta z$ is the projected crystal potential for the thickness Δz. In the case of ordered alloys A–B, this is alternatively written as

$$\begin{aligned} Q(\mathbf{u}) = \delta(\mathbf{u}) &+ \sum_i F^f(\mathbf{u})\,\delta(\mathbf{u} - \mathbf{u}_i^f) \\ &+ \sum_j F^s(\mathbf{u})\,G^s(\mathbf{u})\,\delta(\mathbf{u} - \mathbf{u}_j^s) \end{aligned} \tag{5}$$

and

$$F^f(\mathbf{u}) = i\sigma\Delta z T(\mathbf{u})\,[c_A f_A(\mathbf{u}) + c_B f_B(\mathbf{u})], \tag{6}$$

$$F^s(\mathbf{u}) = i\sigma\Delta z T(\mathbf{u})\,[f_A(\mathbf{u}) - f_B(\mathbf{u})], \tag{7}$$

where $G^s(\mathbf{u})$ is the factor composed of the geometrical structure factor, $T(\mathbf{u})$ the temperature factor, $f(\mathbf{u})$ the scattering factor, and c the unit-cell content. The subscripts indicate the constituent atoms A and B.

For a periodic object, we have a one-dimensional representation,

$$\Psi_n(h) = \sum_{h'} \{\Psi_{n-1}(h - h')\,P(h - h')\}\,Q(h'). \tag{8}$$

The wave function for a superlattice reflection at the nth slice is written by three partial sums E_1, E_2 and E_3,

$$\begin{aligned} &\Psi_n^s(H + h) \\ &= E_1 + E_2 + E_3 \\ &= \sum_{h'} \Psi_{n-1}^f(H + h - h')\,P(H + h - h')\,Q^s(h') \\ &+ \sum_{H'} \Psi_{n-1}^s(H + h - H')\,P(H + h - H')\,Q^f(H') \\ &+ \sum_{h'} \Psi_{n-1}^s(H + h - h')\,P(H + h - h')\,Q^s(h'), \end{aligned} \tag{9}$$

where $\sum_{H'}$ and $\sum_{h'}$ imply the summations for fundamental and superlattice reflections, respectively. The first sum E_1 corresponds to the scattering of fundamental reflections at the $(n-1)$th slice into the superlattice reflections at the nth slice with the vector $\{U_1\}$. The sum E_2 is the scattering of superlattice reflections with the vector $\{U_2\}$, and the sum E_3 the scattering of superlattice reflections into other superlattice reflections with the vector $\{U_3\}$. The structure factor of fundamental reflections is generally larger than that of superlattice reflections, *i.e.*

$$|Q^f| > |Q^s|. \tag{10}$$

It is reasonable to assume that the third term of (9) is negligible in comparison with the sum of the other two, if $|\Psi_{n-1}^s(H + h - h')|$ is sufficiently small. A similar assumption, neglect of double diffuse scattering, is adopted by Spence (1978) in a dynamical image calculation of structure defects. The validity of this assumption will be discussed later.

Based on the above approximation, the wave function of a superlattice reflection at the first slice is given as

$$\begin{aligned}\Psi_1^s(H+h) &= Q^s(H+h)\\ &= F^s(H+h)\,G^s(H+h)\\ &= F^s(H+h)\,G^s(h). \end{aligned} \tag{11}$$

At the second slice, it is given as

$$\begin{aligned}\Psi_2^s(H+h) &= \sum_{h_1} \Psi_1^f(H+h-h_1)\,P(H+h-h_1)\,Q^s(h_1)\\ &\quad + \sum_{H_1} \Psi_1^s(H+h-H_1)\\ &\quad \times P(H+h-H_1)\,Q^f(H_1)\\ &= \sum_{h_1} \Psi_1^f(H+h-h_1)\,P(H+h-h_1)\\ &\quad \times F^s(h_1)G^s(h_1)\\ &\quad + \sum_{H_1} F^s(H+h-H_1)G^s(H+h-H_1)\\ &\quad \times P(H+h-H_1)\,Q^f(H_1)\\ &= G^s(h)\{\sum_{h_1} \Psi_1^f(H+h-h_1)\\ &\quad \times P(H+h-h_1)\,F^s(h_1)\\ &\quad + \sum_{H_1} F^s(H+h-H_1)\\ &\quad \times P(H+h-H_1)\,Q^f(H_1)\}. \end{aligned} \tag{12}$$

Here we used a relationship

$$G^s(h_1) = G^s(H'+h) = G^s(h), \tag{13}$$

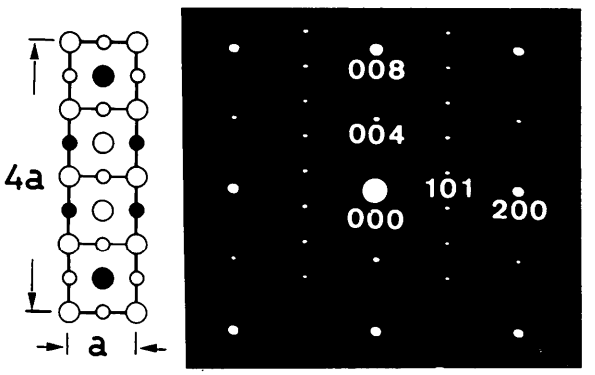

(a) (b)

Fig. 2. (a) Atomic arrangement of the superstructure of $D0_{23}$ type projected along [010]. Open circles are Au atoms and full circles are Cd or Zn or Mg atoms. Large and small circles indicate the atoms at $Y = 0$ and $Y = \frac{1}{2}$, respectively. (b) Electron diffraction pattern of Au_3Cd. The incident beam is parallel to the [010] direction.

because the superlattice reflections have the same geometrical structure factor. At the nth slice, the wave function is generally given as

$$\begin{aligned}\Psi_n^s(H+h) = G^s(h) \Bigg[& \sum_{h_{n-1}} \Psi_{n-1}^f(H+h-h_{n-1})\\ & \times P(H+h-h_{n-1})\,F^s(h_{n-1})\\ & + \sum_{H_{n-1}} \Bigg[\sum_{h_{n-2}} \Psi_{n-2}^f(H+h-H_{n-1}-h_{n-2})\\ & \times P(H+h-H_{n-1}-h_{n-2})\,F^s(h_{n-2})\\ & + \dots\\ & + \sum_{H_2} \Bigg[\sum_{h_1} \Psi_1^f(H+h-H_{n-1}\dots-H_2-h_1)\\ & \times P(H+h-H_{n-1}\dots-H_2-h_1)\,F^s(h_1)\\ & + \sum_{H_1} F^s(H+h-H_{n-1}\dots-H_2-H_1)\\ & \times P(H+h-H_{n-1}\dots-H_2-H_1)\\ & \times Q^f(H_1)\Bigg]_1\\ & \times P(H+h-H_{n-1}\dots-H_2)\,Q^f(H_2)\Bigg]_{n-2}\\ & \times P(H+h-H_{n-1})\,Q^f(H_{n-1})\Bigg]_{n-1}. \end{aligned} \tag{14}$$

This equation shows that the amplitude of superlattice reflection is proportional to the factor $G^s(h)$. If the summations are taken over all values of H and h, the term inside the bracket $[\ ]_{n-1}$ is dependent on $F^s(h)$ and $P(h)$, but independent of Ψ^f and Q^f. For the superlattice reflections at nearly the same value of $|\mathbf{u}_s|$, therefore, the relationship between the wave functions is given as

$$\Psi_n^s(\mathbf{u}')/\Psi_n^s(\mathbf{u}'') \simeq F^s(\mathbf{u}')\,G^s(\mathbf{u}')/[F^s(\mathbf{u}'')\,G^s(\mathbf{u}'')]. \tag{15}$$

This implies that the two beams of superlattice reflection hold a nearly kinematical relationship; the wave functions have almost the same phase and the amplitudes proportional to the respective structure factors. Actually, for the Au_3Cd alloy with the superstructure of $D0_{23}$ type, the nearly kinematical relationship has been found between the superlattice reflections 004 and 110 for the foil thickness up to about 600 Å [Hiraga *et al.*, 1981]. The superstructure of $D0_{23}$ type is shown in Fig. 2(*a*) and the electron diffraction pattern of Au_3Cd is given in Fig. 2(*b*). The

above formulation yields a theoretical background for the observed results.

In this connection, it is worthwhile to consider the conditions in which the kinematical relationship of (15) is realized for binary alloys with the superstructure of $D0_{23}$ type other than Au_3Cd. With the intention of changing the value of $|Q^s(\mathbf{u})|$, we have chosen Au_3Zn and Au_3Mg for comparison with Au_3Cd; the value of $|Q^s(\mathbf{u})|$ increases in the order of the sequence of Au_3Cd to Au_3Zn to Au_3Mg. In the calculation, experimental parameters such as lattice constants were assumed to be the same for the three alloys as in the previous paper (Hiraga *et al.*, 1981). The $D0_{23}$ structure of Au_3Zn actually exists while that of Au_3Mg is only hypothetical for comparison.

In the dynamical calculation described below, we use the transmission function

$$q(x,y) = \exp\,[i\sigma\varphi(x,y)\,\Delta z] \qquad (16)$$

instead of (4) for the weak-phase-object approximation. We discuss first the validity of neglecting the third term in (9) for the three alloys. For the 004 reflection, the ratio of absolute value of the third term to that of the sum of the first and second terms is shown as a function of thickness in Fig. 3. The ratio for Au_3Cd is less than 0·1 over a thickness up to about 700 Å. Consequently, the above assumption is valid for the alloy foils as thick as 700 Å. In this range, the ratio of the amplitude of 004 reflection to 101 reflection, $A(004)/A(101)$, is almost constant and the nearly kinematical relationship holds, as seen in Fig. 4. For Au_3Mg, contrarily, the deviation from the kinematical relationship is appreciable even at thicknesses less than 300 Å; the dynamical interaction of superlattice reflections is so strong that the third term of (9) cannot be neglected even for thin foils. The situation for Au_3Zn shown in Figs. 3 and 4 appears to be intermediate between Au_3Cd and Au_3Mg, being the nearly kinematical relationship held up to 500 Å.

The kinematical relationship of (15) is valid only for the superlattice reflections with $|\mathbf{u}'| \simeq |\mathbf{u}''|$. Fig. 5 shows the ratio of amplitudes of the 004 reflection to the 103 and 105 reflections for Au_3Zn as a function of

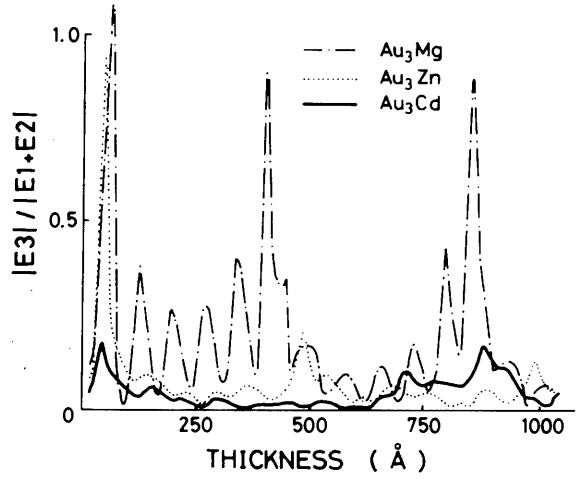

Fig. 3. Ratio of the absolute value of the third term $|E_3|$ in (9) to that of the sum of the other two terms $|E_1 + E_2|$ for Au_3Cd, Au_3Zn and Au_3Mg as a function of crystal thickness.

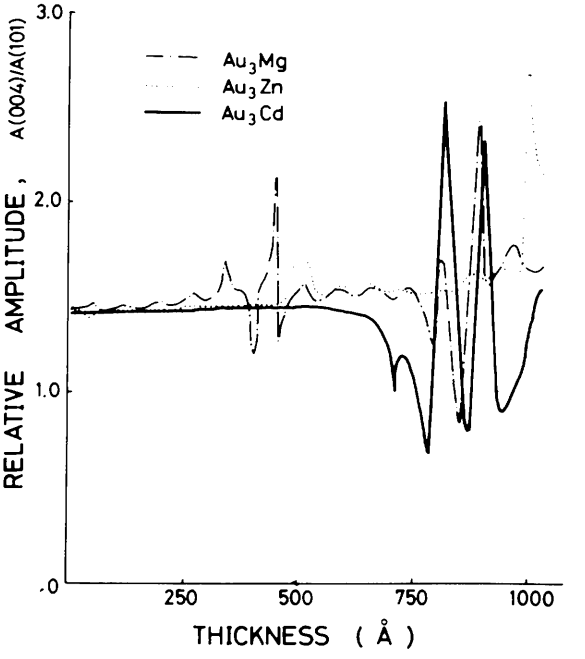

Fig. 4. Relative amplitude of superlattice reflections of 004 and 101 reflections for Au_3Cd, Au_3Zn and Au_3Mg as a function of crystal thickness.

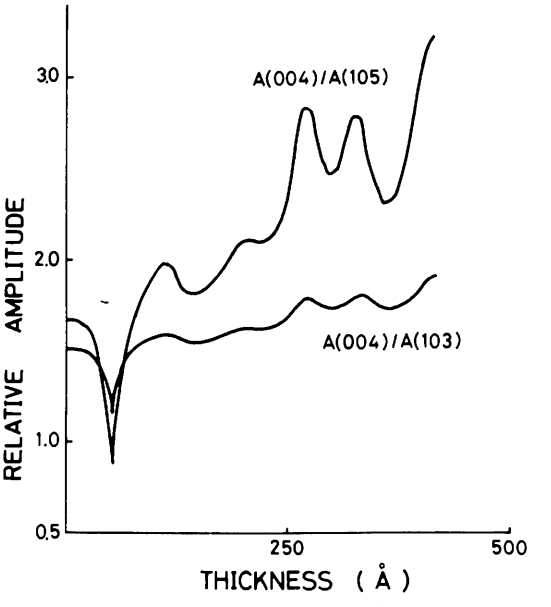

Fig. 5. Relative amplitude of superlattice reflections of 004, 103 and 105 reflections for Au_3Zn as a function of crystal thickness.

crystal thickness. The deviation from the kinematical value is noticeable for 004 *vs* 105 as compared with 004 *vs* 103 as well as 004 *vs* 101.

III. Formation and calculation of superstructure images

On the basis of the above results, let us consider the contrast of superstructure images. The amplitude distribution in the superstructure images is given by

$$\psi(x,y)=\sum_h\sum_k \Psi_n(h,k)\ \exp\left[i\chi(h,k)\right] \times \exp\left[2\pi i(hx/a+ky/b)\right]. \tag{17}$$

Here $\chi(h,k)$ is the phase change due to the transfer function of the objective lens, *i.e.*

$$\chi(h,k)=(\pi/\lambda)\{\Delta f\lambda^2[(h/a)^2+(k/b)^2] -\tfrac{1}{2}C_s\lambda^4[(h/a)^2+(k/b)^2]^2\}, \tag{18}$$

where Δf is the defocus value and C_s is the spherical aberration coefficient. It is alternatively given as

$$\psi(x,y)=A(0,0)\exp\left[i\theta(0,0)\right] \times\left\{1+\sum_h\sum_{k\atop(h,k\neq0)}R(h,k)\exp\left[i\Delta(h,k)\right] \times\exp\left[i\chi(h,k)\right]\exp\left[2\pi i(hx/a+ky/b)\right]\right\}, \tag{19}$$

and

$$R(h,k)=A(h,k)/A(0,0).$$

Here $A(h,k)$ and $A(0,0)$ are the amplitudes of the diffracted beam $hk0$ and the transmitted beam, respectively, and $\Delta(h,k)$ is the phase difference between the two beams,

$$\Delta(h,k)=\theta(h,k)-\theta(0,0). \tag{20}$$

If $\chi(h,k)$ is equal to $\pi/2$ in the optimum conditions, then (19) is given as

$$\psi(x,y)=A(0,0)\exp\left[i\theta(0,0)\right]\left\{1+\sum_h\sum_{k\atop(h,k\neq0)}R(h,k) \times\exp\left\{i[\pi/2+\Delta(h,k)]\right\} \times\exp\left[2\pi i(hx/a+ky/b)\right]\right\}. \tag{21}$$

This holds approximately in a wide range of the spatial frequency 0·20–0·49 Å^{-1} for the 1 MV electron microscope as seen in Fig. 6; important beams of the superlattice reflections for the $D0_{23}$ structure are all involved in this range.

The above equation indicates that the image contrast depends on the phase difference $\Delta(h,k)$. When the kinematical relationship of (15) is satisfied among the superlattice reflections, the intensity distribution of the image $I(x,y)$ is approximately given as

$$A^2(0,0)\left[1-c_1\varphi_s'(-x,-y)\right]=-c_1'\varphi_s(-x,-y)+c_2$$

for $\qquad \Delta(h,k)=\varepsilon(h,k)+\pi/2$

$$A^2(0,0)\left[1+c_1\varphi_s'(-x,-y)\right]=c_1'\varphi_s(x,y)+c_2$$

$$\Delta(h,k)=\varepsilon(h,k)-\pi/2 \tag{22}$$

where c_1, c_1', and c_2 are positive constants, and $\varepsilon(h,k)$ is the phase of the structure factor for $hk0$ reflection. If there is a center of symmetry, $\varepsilon(h,k)$ equals 0 or π. Further, φ_s and φ_s' are written as

$$\varphi_s(x,y)=\frac{1}{i\sigma\Delta zab}\sum_h\sum_k F^s(h,k)\,G^s(h,k) \times\exp\left[-2\pi i(hx/a+ky/b)\right], \tag{23}$$

and

$$\varphi_s'(x,y)=\frac{1}{i\sigma\Delta zab}\sum_h\sum_{k\atop(h,k\neq0)}F^s(h,k)\,G^s(h,k) \times\exp\left[-2\pi i(hx/a+ky/b)\right] =\varphi_s(x,y)-\bar{\varphi}, \tag{24}$$

where $\bar{\varphi}$ is the mean potential.

When the transmitted beam is absolutely extinct at a certain thickness as the result of dynamical interactions with diffracted beams, we may write the amplitude distribution of the image as

$$\psi(x,y)=\sum_h\sum_k A(h,k)\exp\left\{i[\pi/2+\theta(h,k)]\right\} \times\exp\left[2\pi i(hx/a+ky/b)\right] \simeq c_3\varphi_s'(-x,-y), \tag{25}$$

where c_3 is a constant. Thus the intensity distribution of the image is given by

$$I(x,y)=|c_3|^2\left[\varphi_s'(-x,-y)\right]^2. \tag{26}$$

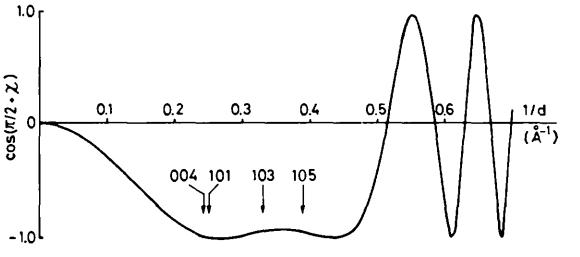

Fig. 6. Real part of the transfer function, $\cos\left[\pi/2+\chi(\mathbf{u})\right]$, at Scherzer condition, for $\lambda=0{\cdot}00872$ Å, $C_s=11$ mm and $\Delta f=1100$ Å.

From the above argument, we conclude that the image intensity depends linearly on $\varphi_s(-x,-y)$ when the transmitted beam is strong, while it is proportional to $[\varphi_s'(-x,-y)]^2$ when the transmitted beam is very weak. Hereafter, the former is called case I and the latter case II.

It is of interest to compare the images for cases I and II of the Au_3Zn alloy. The thicknesses which correspond approximately to each case are indicated in Fig. 7, which shows the amplitude and phase of the transmitted beam and the 004 reflection as a function of crystal thickness. As shown in Fig. 7(*a*) and (*b*), the amplitudes oscillate markedly at a period of about 500 Å; case I is realised at thicknesses of about 400 and 850 Å, and case II at about 230 and 700 Å.

Before the images for the two cases are presented, the calculated results for one-slice thickness (8·24 Å) are shown in Fig. 8. In the image calculation, the Scherzer focus condition (Scherzer, 1949) and the perfect temporal and spatial coherency are provided. In the image of Fig. 8(*a*), the Zn atom positions appear as bright dots. The intensity profile $I(x,y_1)$ agrees well with the curve of $-\varphi_s(x,y_1)$ given by (23) as shown in

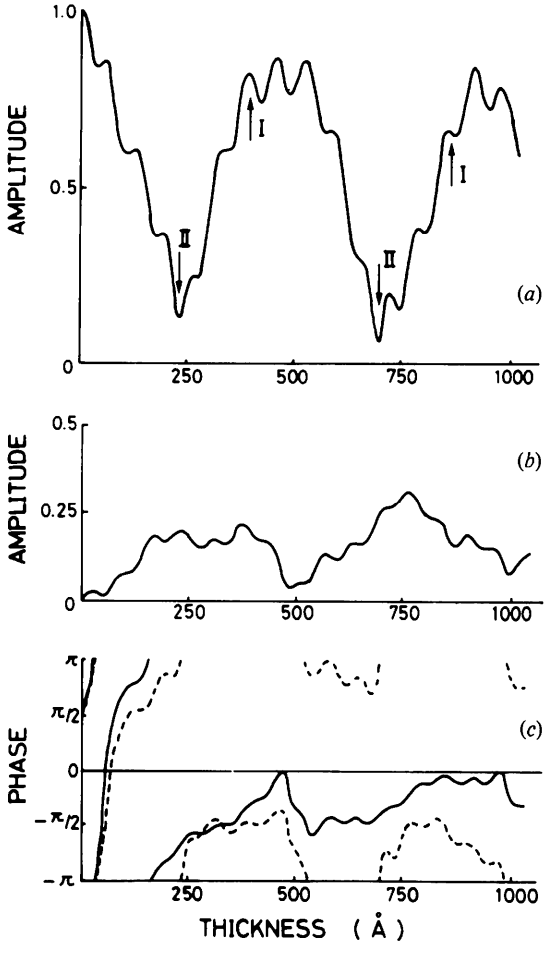

Fig. 7. (*a*) Amplitude of the transmitted beam of Au_3Zn as a function of crystal thickness. Arrows indicate crystal thicknesses corresponding to cases I and II. (*b*) Amplitude of 004 reflection of Au_3Zn. (*c*) Full and dotted lines indicate phase $\theta(h)$ and phase difference $\Delta(h)$ of 004 reflection of Au_3Zn, respectively.

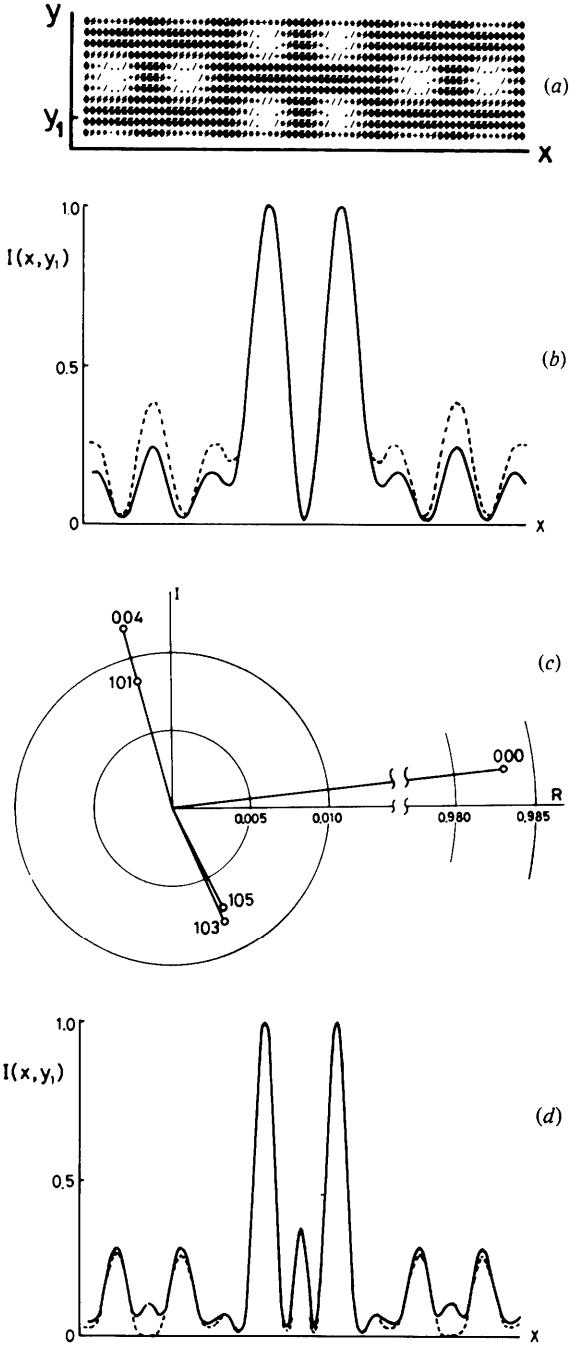

Fig. 8. (*a*) Calculated image of Au_3Zn at 8·24 Å. (*b*) Intensity profile $I(x,y_1)$ of the image (*a*) compared with $-\varphi_s(x,y_1)$ which is marked with a dotted line. (*c*) Amplitude–phase diagram at 8·24 Å (*R*: real, *I*: imaginary). (*d*) Intensity profile $I(x,y_1)$ of the image contributed from only the superlattice reflections. Dotted line indicates $[\varphi_s'(x,y_1)]^2$.

Fig. 8(*b*). The amplitude–phase diagram at this thickness is given in Fig. 8(*c*), which shows that the phase difference between the superlattice reflections and the transmitted beam is almost $\pi/2$ or $-\pi/2$. The intensity profile of Fig. 8(*d*) is calculated by omitting the transmitted beam, which coincides well with that of $[\varphi_s'(x,y_1)]^2$. The intensity profile is much sharper than in Fig. 8(*b*).

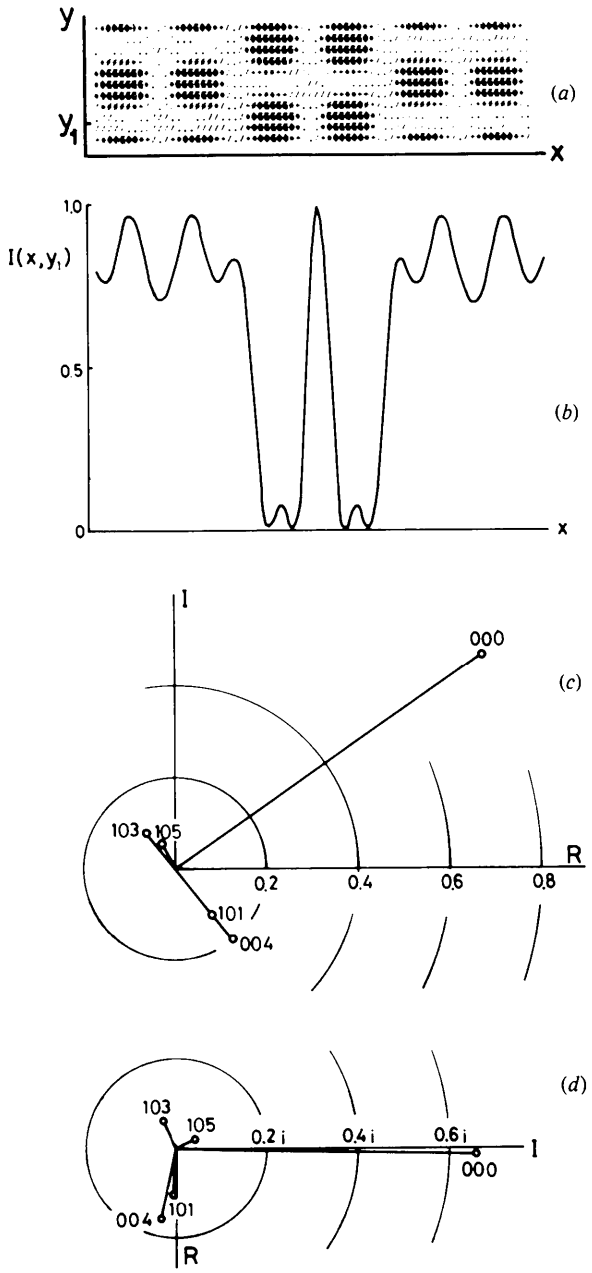

Fig. 9. (*a*) Calculated image for case I of Au_3Zn at 396 Å. (*b*) Intensity profile $I(x,y_1)$ of the image (*a*). (*c*) Amplitude–phase diagram at 396 Å. (*d*) Amplitude–phase diagram at 857 Å.

(*a*) *Case* I

As an example of case I, the image and the intensity profile $I(x,y_1)$ at 396 Å thickness are shown in Figs. 9(*a*) and (*b*), respectively. The Zn atom positions appear as dark dots, and $I(x,y_1)$ is in reverse contrast to Fig. 8(*b*). This is easily understood from the amplitude–phase diagram of Fig. 9(*c*), which indicates that the phase difference $\Delta(h,k)$ for the 004 and 101 reflections is nearly $-\pi/2$; *i.e.* out of phase from the case of very thin crystals. At 857 Å, nearly the same result is obtained, although the deviations from the kinematical relationship are more appreciable than at 396 Å, as seen in Fig. 9(*d*).

(*b*) *Case* II

Fig. 10 shows the calculated results at 231 Å. In this case, the Zn atom positions appear as bright dots, as seen in Fig. 10(*a*). The $I(x,y_1)$ curve of Fig. 10(*b*) is almost the same as the case of the very thin crystal of Fig. 8(*d*). Note in Fig. 10(*c*) that the transmitted beam is absolutely extinct.

The interpretable images are not obtained generally at thicknesses intermediate between cases I and II, since the appropriate conditions for the superstructure images are not satisfied.

IV. Concluding remarks and summary

In the above argument, we have ignored the contribution of fundamental reflections to the superstructure images. However, some beams of the fundamental

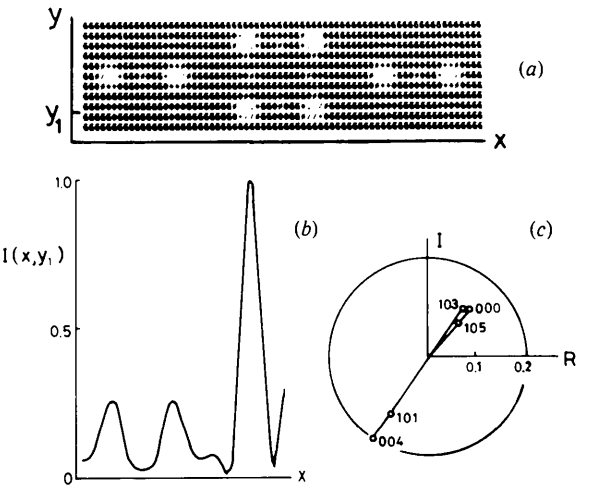

Fig. 10. (*a*) Calculated image for case II of Au_3Zn at 231 Å. (*b*) Intensity profile $I(x,y_1)$ of image (*a*). (*c*) Amplitude–phase diagram at 231 Å.

reflections pass through the objective aperture in the high-resolution observations, and these beams play important roles for imaging the fundamental f.c.c. structure but not for distinctive recognition of constituent atoms in the superstructure images. When these beams are extinct, largely by spherical and chromatic aberration effects, the images can be interpreted straightforwardly in terms of the superstructure, as seen in Figs. 8, 9 and 10. On the other hand, direct interpretation is not always possible when the fundamental reflections are not extinct; no kinematical relationships exist generally between the fundamental reflections and the superlattice ones. Careful comparison of the observation with calculation based on the dynamical scattering theory is necessarily important in such cases.

Also, we should be cautious in interpreting the images of ordered alloys of which the superlattice reflections are fairly strong, because the dynamical interaction among them cannot be neglected. This is the case in Au_3Mg, where the kinematical relationship fails for very thin foils (Figs. 3 and 4). Nevertheless, the conclusions may be summarized as follows.

(1) The superstructure images of binary alloys are observable at certain thicknesses when some superlattice reflections with almost identical magnitudes to the reciprocal-lattice vectors have nearly kinematical relationships; the phases of these reflections are nearly the same and their amplitudes are proportional to the structure factors. The situation holds even at the thickness where the transmitted beam is absolutely extinct.

(2) The above condition is retained at thicker foils when the ordered alloy has a smaller difference in the scattering factors of constituent atoms; the limiting thickness decreases in the order of the sequence of Au_3Cd to Au_3Zn to Au_3Mg for the superstructure of $D0_{23}$ type.

(3) The superstructure image taken only with the kinematically related superlattice reflections reflects the difference in potentials of the constituent atoms projected along the incident beam. The images correspond to difference Fourier syntheses.

(4) When the amplitude of the transmitted beam is relatively large, the image contrast depends sensitively on the phase difference between the superlattice reflections and the transmitted beam. The reverse of contrast with the change in crystal thickness is interpreted in terms of the amplitude–phase diagram.

The author wishes to thank Professor M. Hirabayashi for valuable discussion and advice throughout the work. Thanks are also given to Dr K. Hiraga for his meaningful comments on the manuscript.

References

AMELINCKX, S. (1978–79). *Chem. Scr.* **14**, 197–206.
COWLEY, J. M. (1975). *Diffraction Physics*. Amsterdam: North-Holland.
COWLEY, J. M. & MOODIE, A. F. (1957). *Acta Cryst.* **10**, 609–619.
HIRABAYASHI, M. (1980). *Electron Microsc.* **4**, 142–149.
HIRABAYASHI, M., HIRAGA, K. & SHINDO, D. (1981). *J. Appl. Cryst.* **14**, 169–177.
HIRAGA, K., HIRABAYASHI, M. & SHINDO, D. (1977). *High Voltage Electron Microscopy*—1977, edited by T. IMURA & H. HASHIMOTO, pp. 309–312. Tokyo: Japanese Society of Electron Microscopy.
HIRAGA, K., SHINDO, D. & HIRABAYASHI, M. (1981). *J. Appl. Cryst.* **14**, 185–190.
HIRAGA, K., SHINDO, D., HIRABAYASHI, M., TERASAKI, O. & WATANABE, D. (1980). *Acta Cryst.* B**36**, 2550–2554.
IIJIMA, S. (1971). *J. Appl. Phys.* **42**, 5891–5893.
SCHERZER, O. (1949). *J. Appl. Phys.* **20**, 20–29.
SPENCE, J. C. H. (1978). *Acta Cryst.* A**34**, 112–116.
TERASAKI, O., WATANABE, D., HIRAGA, K., SHINDO, D. & HIRABAYASHI, M. (1980). *Micron.* **11**, 235–240.
VAN TENDELOO, G. (1980). *J. Microsc.* **119**, 125–140.